Advances in Water Resources 161 (2022) 104120

Contents lists available at ScienceDirect

Advances in Water Resources

journal homepage: www.elsevier.com/locate/advwatres

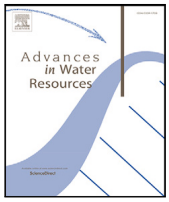

A volume penalization immersed boundary method for flow interactions with aquatic vegetation

Xiao Yu *, Minglan Yu

Department of Civil and Coastal Engineering, Engineering School of Sustainable Infrastructure & Environment, University of Florida, United States of America

ARTICLE INFO

Keywords:
Immersed boundary method
Flow vegetation interactions
Vegetation patch-scale hydrodynamics

ABSTRACT

A volume-penalization immersed boundary (VPIB) method was developed to study flow interactions with aquatic vegetation. The model has been validated with data from laboratory experiments and previous high-fidelity models with satisfactory results. Sensitivity analyzes on both penalty parameter and thickness parameter were conducted, and optimal values for these parameters are recommended. The validated model has been applied to study the effects of swaying motion of vegetation stems on the flow dynamics at both vegetate-stem scale and patch scale. The swaying motion of the vegetation stem is prescribed following a cubic law that peaks at the top and decreases to zero at the bottom. At stem-scale, the hydrodynamics depend on the Keulegan Carpenter number (KC), which is defined as the maximum excursion of the vegetation stem to the diameter of the stem. Simulations with three KC values were carried out. For $KC \geq 1$, the flow turbulence is significantly enhanced by the swaying motion of the stem, and turbulence becomes more isotropic in the wake. The swaying motion of vegetation stems caused a 5% increase of the bottom shear stress at the shoulders of the stem, and the effect is negligible in the wake. At patch-scale, the hydrodynamics depend on the effective Keulegan Carpenter number based on the patch size of the vegetation patch, and the solid volume fraction for dense vegetation canopy. Solid volume fraction was varied while maintaining the same effective Keulegan Carpenter in the simulations. When the effective Keulgen Carpenter number is small ($KC < 1$), effects of the swaying motion of vegetation stems on the large patch-scale dynamics are not significant, including both the turbulence statistics and the bottom stress.

1. Introduction

Aquatic vegetation provides many important ecological services (Micheli and Kirchner, 2002; Kremen, 2005), including shoreline protection, nursery areas for fish, shellfish and crustaceans, and water quality improvement. Aquatic vegetation stabilizes coastal shorelines, prevents erosion and traps sediment to promote intertidal accretion to keep up with sea-level rise. However, due to human activities (Gedan et al., 2009) and the threat of sea-level rise (Craft et al., 2009), a large amount of aquatic vegetation has been lost in recent decades (Marani et al., 2011). On the other hand, aquatic vegetation has been widely used as cost-effective coastal defense systems to protect coastal communities (Gedan et al., 2011) against the increased storminess and accelerated sea-level rise. It is of critical importance to understand the hydrodynamics and sediment transport processes in vegetated regions for aquatic vegetation conservation and restoration, because the evolution of estuarine and coastal morphology in vegetated regions strongly depends on the interplays of flow, vegetation and sediment accretion.

In emergent vegetation canopy, plant stems fill the entire water column. When flow enters the vegetation canopy, the mean flow velocity is reduced by drag and sediment carried into the canopy starts to settle. The additional drag exerted by plants is commonly parameterized by a friction coefficient, which is an important parameter in large-scale circulation models and storm surge models to accurately predict the flow attenuation in rivers and estuaries by vegetation. On the other hand, vortices shed from the plants can enhance the turbulence in vegetation canopy. Vegetation generated turbulent eddies could interact with sediment bed, resuspend sediment and enhance sediment transport (Tinoco and Coco, 2013; Yang et al., 2016). At vegetation-stem scale, when flow passes a single isolated vegetation stem, the formation of horseshoe vortex in front of the plant and the unsteady vortex shedding behind the plant are the key hydrodynamic processes. Numerical simulations and laboratory experiments (Zhao et al., 2010; Chen et al., 2017) have been carried out to understand the flow structure and sediment transport around circular cylinders. The entrainment and erosion of sediment near a circular cylinder strongly depend on the turbulence generation mechanisms. Due to complex interactions of both cylinder-generated and wall-generated turbulent eddies with the sediment bed, accurate

* Corresponding author.
E-mail address: xiao.yu@essie.ufl.edu (X. Yu).

https://doi.org/10.1016/j.advwatres.2021.104120
Received 18 May 2021; Received in revised form 17 December 2021; Accepted 24 December 2021
Available online 10 January 2022

sediment transport model around a single vegetation stem represented by a circular cylinder has yet to be developed, which is important for soil erosion control.

Aquatic vegetation often grows in patches and heterogeneous plant forms. Understanding flow interactions with a patch of emergent vegetation, including flow attenuation by vegetation, turbulent mixing and sediment transport, is of critical importance for natural resources management. Laboratory experiments (Zong and Nepf, 2012; Shan et al., 2020) and numerical simulations (Chang and Constantinescu, 2015) show that bleeding flow develops in a sparse vegetation canopy and large-scale wake billows form in a dense vegetation canopy. Three distinct flow regimes have been identified by Nicolle and Eames (2011) based on the solid volume fraction (SVF) of vegetation. At low solid volume fraction ($SVF < 0.05$), individual vegetation stems behave like isolated single stems. At intermediate solid volume fraction ($0.05 < SVF < 0.15$), a shear layer is generated at the shoulder of the patch. Large-scale wake billows are shed in the wake of the patch. At high solid volume fraction ($SVF > 0.15$), the array of vegetation stems generates a wake in a similar way to a solid body of the same shape of the vegetation patch. The sediment transport within and around the vegetation patch is directly linked with the hydrodynamic processes. For sparse vegetation canopy, the flow accelerates between vegetation stems and intensive erosion occurs within the canopy due to stem-scale turbulence. For dense vegetation canopy, the large patch-scale wake billows dominate the sediment transport, leading to a scour hole around the patch.

Process-based models have been widely used to provide insights on interplays among flow, vegetation and sediment. Most previous numerical model studies on flow and sediment transport in emergent vegetation canopy treat vegetation stems as regularly-spaced or staggered rigid circular cylinders (Stoesser et al., 2010; Huai et al., 2015), and only a few stems can be implemented due to the available computational resources. However, emergent vegetation stems are flexible, and move back and forth by waves and wind, which can stir water and possibly sediment. In addition, the spatial distribution of vegetation stems is heterogenous and the collective friction effects of vegetation due to drag play important roles in the dynamics. With recent advancement in computational methods (Uhlmann, 2005; Lee and Choi, 2015), a massively-parallel high-fidelity model that can efficiently simulate flow interactions with moving deforming vegetation needs to be developed.

To model the fluid structure interaction, two approaches have been developed. One approach is to move the computational mesh to follow the motion of the solid object. Based on the relation between the motion of the computational grid and the motion of the fluid, either Lagrangian or Eulerian framework is used. In Lagrangian framework, the local fluid velocity is used to move the computational mesh. In Eulerian framework, velocity on a separate fixed Eulerian mesh is used to move the computational mesh. The motion of the computational mesh can cause severely distorted mesh of poor quality under the Lagrangian framework. Arbitrary Lagrangian–Eulerian (ALE) method (Hirt et al., 1974) combines both Lagrangian and Eulerian framework, after the explicit Lagrangian update of the computational mesh with the updated solution, a new mesh with better quality is defined by moving the mesh at a specified velocity, and the Lagrangian solution is transferred conservatively onto the new mesh (Berndt et al., 2011). ALE technique is easy to implement and accurate; however, for problems with large translations or rotations, the computational mesh tends to be ill-shaped, which affects the accuracy of the solution. In addition, the remeshing can be expensive to compute.

The other approach is to not make any changes of the fluid mesh. A widely used method is the immersed boundary (IB) method (Peskin, 2002). The solid object interacts with the fluid through the local body forces applied to the fluid at the point locations at the fluid–solid interface to enforce the boundary conditions at the solid surface. One of the advantage of IB method is that the mesh generation is greatly simplified. The generation of body fitting computational grid can be difficult for complex geometries and grid quality deteriorates with complexity of the geometry using unstructured grids. For IB method, block structured grids with local refinement can be used, which are computationally efficient. One of the drawbacks of IB method is the smear of the interface compared to the body-fitting approach. The counterpart of the IB method for finite element or spectral element methods is the fictitious domain method (Glowinski et al., 1994; Parussini and Pediroda, 2009). The coupling between the fluid and solid phase is done by constraining fluid and the solid body at the interface using a Lagrangian multiplier that represents the body forces.

Two approaches, namely the direct forcing and the feedback forcing methods, have been developed for the IB method (Mittal and Iaccarino, 2005). In the classical IB method (Peskin, 2002), the direct forcing method, Lagrangian markers are used to describe the solid surface. The IB methods use a distribution function to interpolate the fluid velocity from the Eulerian fluid grids to the Lagrangian markers to calculate the body force term (Tseng and Ferziger, 2003). The forcing is then spread from the Lagrangian markers to the surrounding Eulerian fluid grids via a smooth kernel function (Wang and Liu, 2004). To conserve the total force and torque, different algorithms have been developed for both uniform and nonuniform Eulerian grids (Akiki and Balachandar, 2016). The classical IB method is second order accurate at the solid surface. The classical IB method poses a stiff problem and results in a small computational time step, which severely restricts the simulation. In addition, the implementation of the IB method can be difficult and the accuracy of the method also depends on the distribution of Lagrangian markers. On the other hand, the volume penalization immersed boundary (VPIB) method, a feedback forcing method, simply represents solid bodies as porous medium with very small permeability and can be used in conjunction with high-order numerical schemes (Kadoch et al., 2012; Piquet et al., 2016). The implementation of the VPIB method is of minimum effort by replacing the implementation of no-slip boundary condition on the solid surface with a simple source term in the Navier–Stokes equation. The VPIB method is also computationally more efficient without the need to calculate the coupling forcing terms between fluid and solid directly.

Emergent vegetation is commonly modeled as rigid circular cylinder, and the frictional dissipation due to vegetation is parameterized by a drag coefficient. For marsh grass, the Reynolds number based on the stem size and current/wave velocity is on the order of $O(100 \sim 1000)$. For a single circular cylinder, a drag coefficient around 1 is often used. Due to flow sheltering in vegetation canopy, the drag coefficient also depends on the solid volume fraction (Nepf, 1999; Tanino and Nepf, 2008; Augustin et al., 2009). In natural environments, emergent vegetation plants are flexible, and they sway on wind. The forced motion of the plant could stir the water column and affect the drag, turbulent mixing and sediment transport. On the other hand, the marsh grass is stiff with a large Cauchy number (defined as the ratio of the elastic restoration force to the hydrodynamic drag force). The movement of the vegetation stem is relatively small. In this study, we focus on the parameter range of small Keulegan–Carpenter number, which is defined as the ratio of the maximum excursion of the vegetation motion to the diameter of the vegetation stem. A simplified prescribed motion of the vegetation is implemented to simulate the forced motion of the vegetation plant. We focus on how the forced motion of vegetation affects the drag and turbulent mixing in the emergent vegetation canopy.

This paper is organized as follows. First, we present the governing equations for the volume penalization immersed boundary method and the numerical schemes. Next, we extensively validate the method by comparing the numerical simulation results with data from previous laboratory experiments and high fidelity numerical simulations. The validated model is then applied to investigate how a simplified prescribed swaying motion of vegetation affects flow turbulence and bed shear stress under steady current at both stem- and patch-scales.

2. Governing equation and numerical method

In the volume penalization immersed boundary method, the solid objects, such as vegetation stems, are modeled as porous media with low permeability. The governing equations are given as follows:

$$\frac{\partial u_i}{\partial x_i} = 0, \tag{1}$$

$$\frac{\partial u_i}{\partial t} + \frac{\partial u_i u_j}{\partial x_j} = -\frac{1}{\rho}\frac{\partial p}{\partial x_i} + \nu\frac{\partial^2 u_i}{\partial x_j \partial x_j} + \alpha\epsilon^{-1}(u_i - u_{s,i}), \tag{2}$$

where ρ is the fluid density, ν is the kinematic viscosity of the fluid and p is the dynamic pressure. x_i, u_i and $u_{s,i}$ are the ith component of the position vector, fluid velocity vector and the solid object velocity vector. $i = 1, 2, 3$ represents the streamwise, spanwise and vertical direction, respectively. The penalty parameter ϵ can be interpreted as permeability and a very small value is often implemented. To find the optimal value for the penalty parameter ϵ, a sensitivity analysis needs be conducted.

α is the mask function, defined as

$$\alpha(\mathbf{x}, t) = \begin{cases} 1 & \mathbf{x} \in \Omega_s, \\ 0 & \mathbf{x} \in \Omega_f, \end{cases} \tag{3}$$

where Ω_s is the solid phase and Ω_f is the fluid phase. The no-slip boundary conditions at the fluid–solid interface are no longer included. The solid object is represented by the mask function α. To avoid numerical instabilities, a smoothly transition of the mask function α at the solid–liquid interface with values between 0 and 1 is required. The thickness of the transition layer is defined by δ. The thickness parameter δ measures the spreading of the influences from the solid structure (such as forces or stresses) to the fluid, and is determined based on the grid spacing.

In the present work, we use an analytical expression for the mask function, which can be easily resampled on the fluid grid. The 1D smoothed Heaviside function is implemented as

$$H(x) = \frac{1}{2}\left[\mathrm{erf}\left(\frac{x - x_0}{\delta}\right) + 1\right]. \tag{4}$$

The smoothed Heaviside function provides a good way to alleviate numerical instabilities at the sharp fluid–solid interface. The fluid–solid interface is located at x_0, and the solid is at $x \geq x_0$. For 3D problems, the tensor product of 1D Heaviside function is used at the fluid–solid interface. The sensitivity analysis of the thickness parameter δ needs to be conducted to determine the optimal value of δ.

In large eddy simulation (LES), the large energy containing eddies are resolved and only small sub-grid turbulent eddies are modeled with an appropriate subgrid closure. LES can accurately predict the unsteady vortex shedding of flow around solid object (Zedler and Street, 2001; Kim et al., 2004). In LES, the velocity is decomposed as $u_i = \tilde{u}_i + u_i'$, with $\tilde{u}_i$ as the resolved velocity component and u_i' as the unresolved subgrid velocity component. The governing equation with LES turbulent closure can be written as

$$\frac{\partial \tilde{u}_i}{\partial x_i} = 0, \tag{5}$$

$$\frac{\partial \tilde{u}_i}{\partial t} + \frac{\partial \tilde{u}_i \tilde{u}_j}{\partial x_j} = -\frac{1}{\rho}\frac{\partial \tilde{p}}{\partial x_i} + \frac{\partial \tau_{ij}}{\partial x_j} + \alpha\epsilon^{-1}(\tilde{u}_i - u_{s,i}), \tag{6}$$

in which the shear stress τ_{ij} is the sum of the viscous stress and turbulent stress. Following the Boussinesq eddy viscosity assumption

$$\tau_{ij} = 2(\nu + \nu_{sgs})S_{ij}, \tag{7}$$

where ν_{sgs} is the subgrid eddy viscosity, and $S_{ij} = \frac{1}{2}(\frac{\partial \tilde{u}_i}{\partial x_j} + \frac{\partial \tilde{u}_j}{\partial x_i})$ is the strain rate tensor of the resolved velocity field.

Eddy viscosity ν_{sgs} is given by the Wall Adaptive Local Eddy (WALE) model

$$\nu_t = \Delta_s^2 \frac{(S_{ij}^d S_{ij}^d)^{3/2}}{(S_{ij}S_{ij})^{5/2} + (S_{ij}^d S_{ij}^d)^{5/4}}, \tag{8}$$

with

$$\Delta_s = C_w V_c^{1/3}, \tag{9}$$

$$S_{ij}^d = \frac{1}{2}(g_{ij}^2 + g_{ji}^2) - \frac{1}{3}\delta_{ij}g_{kk}^2, \tag{10}$$

$$g_{ij} = \frac{\partial \tilde{u}_i}{\partial x_j}. \tag{11}$$

The constant C_w is 0.325 and V_c is the volume of the grid cell.

We implemented the volume penalization immersed boundary method in OpenFOAM (Weller et al., 1998). Due to the small value of the penalization parameter ϵ, the momentum equation is a stiff equation. The explicit treatment of the source term $\epsilon^{-1}\alpha(u_i - u_{s,i})$ requires an extremely small time-step of $\Delta t < \epsilon$ (Engels et al., 2015). To alleviate the computational demands, the source term is modeled implicitly. A second order upwind scheme is used as the spatial discretization. The volume penalization IBM is only first order accurate in time, and hence the first-order backward Euler method is used for time marching. The Pressure-Implicit with Splitting of Operators (PISO) algorithm is used to solve the filtered unsteady Navier–Stokes equations. The time step limited by the CFL criterion with the maximum CFL number of 0.5 for all simulations.

3. Model validation

3.1. Turbulent flow over circular cylinder at Re = 3900

Parnaudeau et al. (2008) carried out experimental and LES studies of the flow over a circular cylinder at Reynolds number 3900. Here, we used the experimental data to validate the Volume Penalization Immersed Boundary (VPIB) model for fully developed turbulent flow, in terms of both the mean flow and turbulence statistics. The incompressible Navier–Stokes equations are solved on a regular Cartesian grid. The size of computational domain is 20 D by 10 D by πD in the streamwise (x), spanwise (y) and vertical (z) direction, respectively, in which D is the diameter of the circular cylinder. A constant flow of U_c is imposed at the inlet of the computational domain and outflow boundary condition is implemented at the exit. The outflow boundary condition is a mixed boundary condition. When the fluid flows out of the domain at the boundary, the velocity gradient is set to zero. When the fluid is flowing into the domain, the flow velocity is set to zero so there is no backflow at the boundary. Periodic boundary conditions are applied in both the spanwise (y) and the vertical (z) directions. The circular cylinder is located at $3.4D$ downstream from the inlet and $5D$ from the lateral boundaries. A fixed time step is used with maximum CFL number below 0.5. Uniform grid spacing was used in all three directions, and the grid spacings in the horizontal directions are the same ($\Delta x = \Delta y$).

Numerical simulations with three different grid-resolutions were conducted by varying the ratio of cylinder diameter to the horizontal grid spacing $D/\Delta x$. The vertical grid resolution was kept the same for all three cases with $\Delta z/D \approx 0.065$, which is similar to the LES simulation in Parnaudeau et al. (2008). We first ran each of the simulation for 50 eddy turnover times (D/U_c) to make sure the flow reached equilibrium. The simulation was continued for another 50 eddy turnover time for data analysis. The penalty parameter was kept the same for all three simulations ($D/U_c\epsilon = 25{,}000$) and the thickness parameter (δ) was kept the same ($\Delta x/\delta = 1.3$, 4.0 and 7.0 for the coarse, medium and fine grid resolution, respectively). Results from cases with medium resolution ($D/\Delta x = 24$) and fine resolution ($D/\Delta x = 40$) agree well with each other. For the case with coarse resolution, only 8 grid points were used in each horizontal directions ($D/\Delta x = 8$), model results

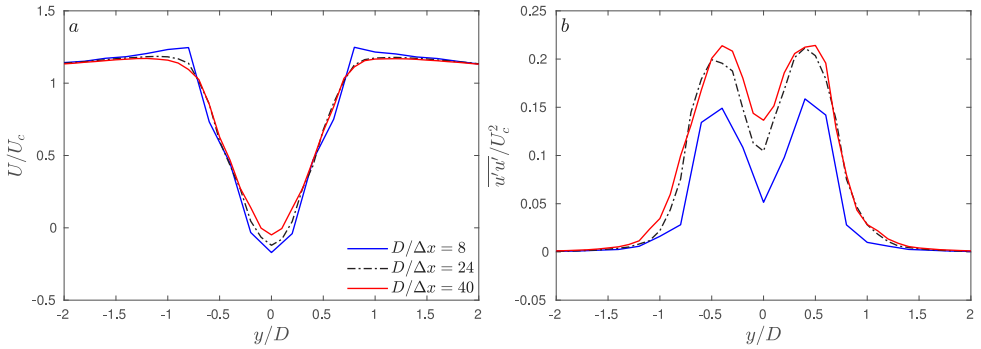

Fig. 1. Grid convergence analysis. The grid resolution is represented by the ratio of the diameter of the cylinder to the horizontal grid spacing (D/Δ). (a) The normalized streamwise (x-) velocity (U/U_c) at $x/D = 2.02$, and (b) the corresponding normalized normal stress $\overline{u'u'}/U_c^2$.

slightly over-predicted the mean streamwise velocity near the shoulder of the circular cylinder in the wake (Fig. 1a) and under-predicted the streamwise (x-) component of the turbulent fluctuation (Fig. 1b). The medium grid resolution with $D/\Delta x = 24$ was used for further model validation and analysis.

Previous studies of the volume-penalization IBM method have evaluated the sensitivity of the penalty parameter (ϵ) and the thickness parameter (δ) with laminar flows and showed it is unlikely to find the optimal value of the penalty parameter ϵ in cases where no reference solution exists Engels et al. (2015). In this study, we focus on the model performance for fully developed turbulent flows at high Reynolds number without reference solution. Fig. 2 panel a and b show the comparison of simulation results with different penalty parameters with the same thickness parameter ($\Delta x/\delta = 4$). The penalty parameter is normalized as $D/U_c\epsilon$ because the flow through porous media depends on the incoming flow speed. The flow through the porous media decreases with ϵ, and converges with sufficient large $D/U_c\epsilon$. When the parameter ϵ is too large (i.e., too permeable), the model significantly under predicted the velocity defect in the wake (Fig. 2a) and the streamwise turbulent fluctuation (Fig. 2b). There is only a slight change from $D/U_c\epsilon = 25{,}000$ to 250,000. Ideally, a small value ϵ is preferred; however, the time step is restricted by ϵ even for the implicit scheme. In this study, $D/U_c\epsilon = 25{,}000$ is chosen.

Fig. 2 panels c and d show how the thickness parameter δ affects the model performance. The thickness parameter depends on the grid spacing and is therefore normalized as $\Delta x/\delta$. The penalty parameter is kept the same for all three simulations. With small $\Delta x/\delta$ (or large δ), the mask function spreads wider, and hence the volume occupied by the solid object is expanded. The model under predicts the velocity defect (Fig. 2c) in the wake and over predicts the streamwise turbulent fluctuation (Fig. 2d). Due to the expansion of the solid object by the mask function, the solid object in the simulation domain appears larger than the actual solid object. The difference between $\Delta x/\delta$ of 4 and 8 is not pronounced. Further increasing $\Delta x/\delta$ can cause numerical instabilities at the fluid–solid interface, and the ratio $\Delta x/\delta \approx 4 \sim 8$ is recommended. In this study, $\Delta x/\delta = 4$ is chosen.

The VIBM model is then validated against laboratory experiment data in detail. The power spectrum of the velocity at numerical probe locations was used to obtain the shedding frequency, the Strouhal number from the LES simulation is $St = 0.21$ compare to $St = 0.208 \pm 0.001$ from the hot wire laboratory experiment data of Parnaudeau et al. (2008). Fig. 3 shows the comparison of the VPIB LES model predictions of the streamwise (x-) velocity with the laboratory experiment at three different downstream locations. Numerical model predicted the strong velocity defect in the recirculation region with a U-shape close to the cylinder, which evolves into a V-shape profile further downstream. The model slightly over-predicted the mean velocity at $x/D = 1.06$ and $x/D = 1.54$ at the shoulder of the cylinder, and under-predicted the velocity defect in the wake at $x/D = 2.02$. The comparison of the spanwise (y-) component velocity is presented in Fig. 3 panel b, d and f. The model results show a anti-symmetry shape with respect to $y = 0$ (center of the cylinder). Model results agree reasonably well with the experiment data and previous LES studies (Kravchenko and Moin, 2000; Parnaudeau et al., 2008). Discrepancies at locations very close to the circular cylinder arise due to the smearing of the fluid–solid interface by the immersed boundary method.

Model results of the streamwise (x-) component of the velocity fluctuation are compared with the laboratory experiment of Parnaudeau et al. (2008) ("·" symbols) of and Lourenco (1993) ("+" symbols) in Fig. 4. At $x/D = 1.06$ the profile shows two strong peaks due to the transitional state of the shear layers. The model underestimated these peaks compared to the laboratory experiment, possibly due to smearing of the fluid–solid interface again. The model underpredicted the peak of the streamwise normal turbulent stress by about 50% at $x/D = 1.06$ and 20% at $x/D = 1.54$. At $x/D > 1.06$, these two peaks of the shear layer are overlapped by two large peaks, and the model results agree well with experimental data. The VPIB method with LES closure generates satisfactory results and can be used to study the turbulence generation mechanisms of emergent vegetation stems.

3.2. Flow over a patch of emergent vegetation

Aquatic vegetation often grows in patches. Flow interactions with a patch of emergent vegetation play important roles in the hydrodynamics. How the solid volume fraction of the vegetation patch and the spatial arrangement of vegetation stems in the patch affect the hydrodynamics is one of the challenging research questions. Here, we conducted a simulation of flow over a circular array of rigid circular cylinders to evaluate the model performance for flow over vegetation patches.

The length, width and height of the computational domain are set to $15D$, $10D$ and πD, respectively, in which D is the diameter of the vegetation patch. A constant flow of U is imposed at the inlet of the computational domain and a outlet boundary condition is implemented at the exit in the streamwise (x-) direction. Periodic boundary condition is implemented in the vertical (z-) direction. Open boundary condition with zero gradient of the velocity is implemented in the spanwise (y-) direction. The Reynolds number based on the patch diameter and current velocity is $Re_D = UD/\nu = 10{,}000$. The vegetation stem size is $d = 0.048D$. The solid volume fraction is 0.023 with 10 stems and 0.05 with 21 stems in the circular patch. Three levels of grid refinement were used, with the finest grid spacing of $\Delta x = \Delta y = d/8$ in the vegetation patch, the coarsest grid spacing much away from the vegetation patch is close to d. The grid resolution is similar to Chang and Constantinescu (2015). A fixed time-step was chosen with $CFL \leq 0.5$. After the solution became steady, statistics were collected over 50 eddy turnover times (D/U). Model results have been compared with laboratory experiment data and previous LES model results (Zong and Nepf, 2012; Chen et al., 2012; Chang and Constantinescu, 2015). VIBM model (Fig. 5) shows satisfactory performance in terms of both the mean velocity

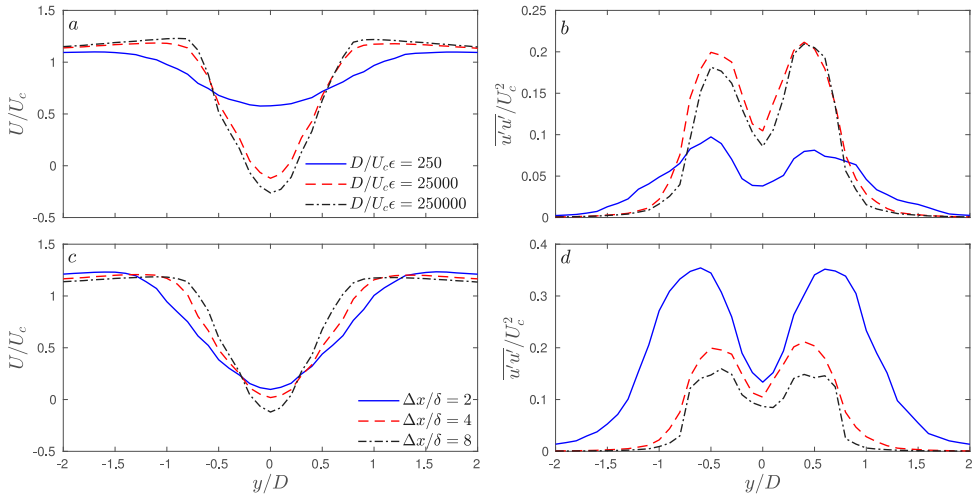

Fig. 2. Sensitivity analyzes of parameters ϵ and δ. Comparison of (a) the normalized streamwise velocity U/U_c and (b) the normalized normal stress component $\overline{u'u'}/U_c^2$ with different penalization parameter ϵ. Comparison of (c) U/U_c and (d) $\overline{u'u'}/U_c^2$ with different thickness parameter δ.

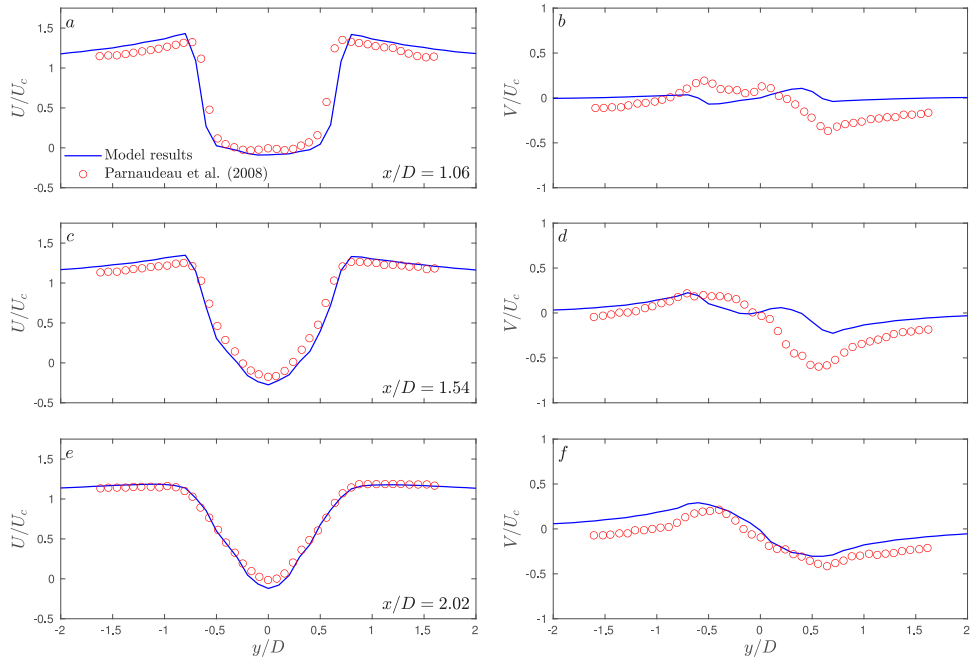

Fig. 3. The normalized streamwise mean velocity (U/U_c) at different location, (a) $x/D = 1.06$, (c) $x/D = 1.54$, (e) $x/D = 2.02$. (b), (d) and (f) are the corresponding normalized spanwise mean velocity (V/U_c). The center of the cylinder is located at $x/D = 0$. The velocity is normalized by the undisturbed current velocity U_c at the inlet.

(u/U) and turbulence statistics (the root mean square of the streamwise component of the velocity fluctuation u_{rms}/U) even with a relatively coarse resolution of $d/\Delta x = 8$.

3.3. Flow generated by an oscillating circular cylinder

To evaluate the performance of VPIB model for moving objects, we conducted numerical simulations of flow generated by an oscillating cylinder at low Keulegan–Carpenter number. Model results were compared with experimental data by Dutsch et al. (1998). The Keulegan–Carpenter number is defined as

$$KC = \frac{U_{max}}{\omega D}, \tag{12}$$

where U_{max} is the maximum velocity of the cylinder motion, ω is the angular frequency of the oscillatory motion and D is the diameter of the cylinder.

We set up a two–dimensional simulation with computational domain size of $55D$ in the streamwise direction and $35D$ in the spanwise direction. Open boundary conditions with zero gradient of velocities were implemented in both lateral directions. The computational domain is sufficiently large so that the flow around the moving cylinder is not affected by the boundaries. Initially, the circular cylinder is located at the center of the computational domain. It oscillates with the time-dependent velocity of $u_{cyl} = U_{max}\cos(\omega t)$ in x direction. The Reynolds number is 100 and the Keulegan Carpenter number (KC) is 5. Cartesian grid with uniform size of $\Delta x/D = \Delta y/D = 0.05$ was implemented. The permeability parameter was set to $\epsilon = 10^{-5}$ s^{-1} in this simulation. The thickness parameter δ was set to $\Delta x/\delta = 8$. A fixed time step was used with the maximum CFL number below 0.5. Fig. 6 shows the comparison between model results and laboratory data at four different locations at wave phase $\omega t = 0$, when the cylinder is located at its origin. The model predicts the U-shaped velocity profile with two peaks near the edge of the cylinder at location $x/D = 0$. The U-shaped velocity

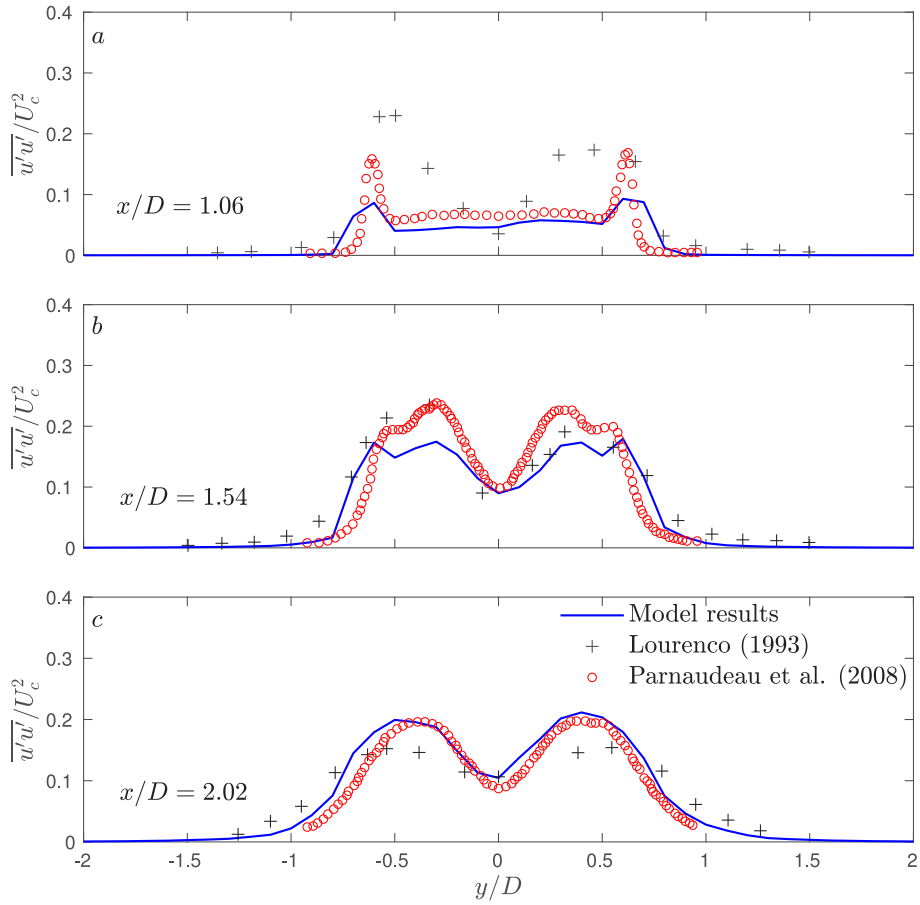

Fig. 4. The normalized normal stress component $\overline{u'u'}$ at different location, (a) $x/D = 1.06$, (b) $x/D = 1.54$, (c) $x/D = 2.02$.

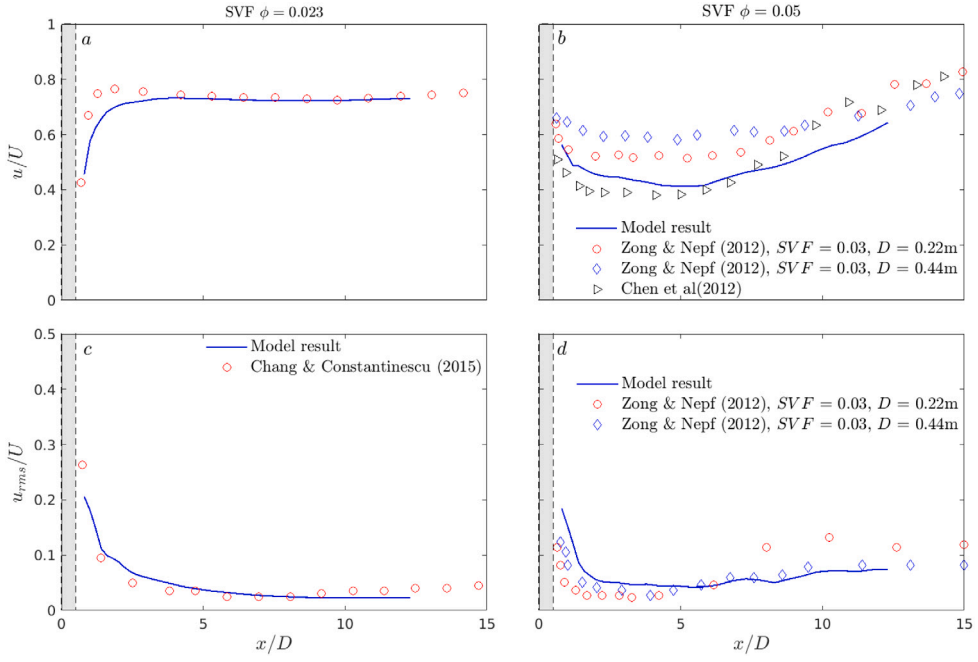

Fig. 5. Model validation of flow over a circular patch of emergent rigid cylinders. The gray region indicates the circular porous patch. The normalized mean streamwise (x-) velocity u/U for flow over a patch with solid volume fraction of (a) $\phi = 0.023$ and (b) $\phi = 0.05$. The normalized streamwise (x-) component of turbulent fluctuation u_{rms}/U for flow over a patch with solid volume fraction of (c) $\phi = 0.023$ and (d) $\phi = 0.05$.

profile evolves into a V-shaped profile at $x/D = 0.6$, which smooths out further downstream at $x/D = 1.2$. For spanwise velocity component, the antisymmetry of velocity profile around $y/D = 0$ can be observed. The

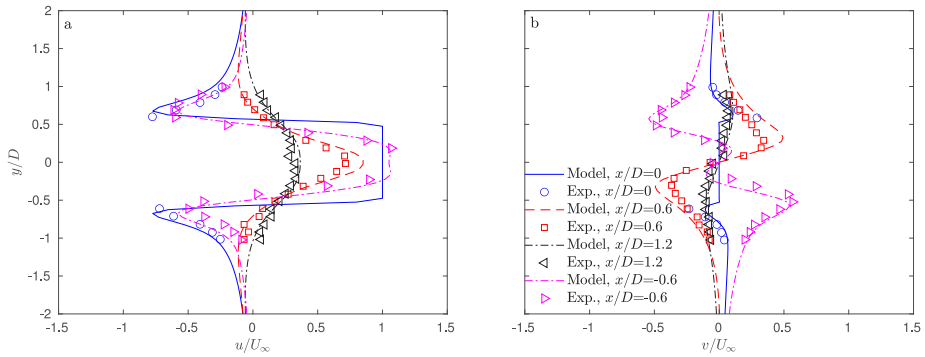

Fig. 6. The velocity at $\omega t = 0$ at different locations. (a) the inline component velocity (x-component), (b) the transverse component velocity (y-component).

model results agree well with laboratory experiment data, and the VPIB method is capable to capture flow interactions with moving objects.

4. Effect of swaying motion of vegetation on stem-scale flow structures

Wetlands are highly complex environments with emergent vegetation that is rooted underwater but emerges through the air–water interface. On one hand, emergent vegetation attenuates waves and shields the water surface from wind. On the other hand, emergent plants sway in wind because of wind-plant interactions and stir the water column, which could enhance turbulent mixing and sediment transport.

4.1. Simulation setup

A single vegetation stem is placed in the turbulent channel flow. The motion of the vegetation is mainly driven by the wind interaction with the part of the plant above the water, and we prescribed the motion of the underwater part of vegetation for simplicity. The vegetation stem is modeled as a cantilever beam with the force applied at the top of the submerged portion of the vegetation stem. For stiff vegetation, effects of hydrodynamic force on structure deformation could be negligible. For simplicity, we implemented a one-way coupling scheme to model the fluid–structure interaction. Only the displacement of the structure is transferred to the fluid solver, and the fluid pressure acting on the structure is not transferred to the structure solver. Based on the elastic beam theory, the deflection at any beam section is

$$\delta_x(z) = \frac{Fz^2}{6EI}(3H - z), \tag{13}$$

where F is the magnitude of the force, E is the Young's Modulus, I is the area moment of inertia of the beam, H is the water depth, and δ_x is the deflection of the beam at vertical elevation z.

The swaying motion is modeled by an oscillating force $F(t) = F_m \sin(\omega t)$ with ω as the angular frequency. In this study, we use the maximum displacement δ_{max} to characterize the stem motion as

$$\delta_x(z,t) = \delta_{max} \sin(\omega t)\frac{z^2}{2H^2}\left(3 - \frac{z}{H}\right). \tag{14}$$

The velocity of the stem can therefore be derived as

$$u_s(z,t) = \omega\delta_{max} \cos(\omega t)\frac{z^2}{2H^2}\left(3 - \frac{z}{H}\right). \tag{15}$$

The Keulegan Carpenter number is defined as $KC = u_{max}/\omega D = \delta_{max}/D$.

The size of the computational domain is $6.4H \times 3.2H \times H$, where H is the depth of the channel. The computational domain is sufficiently large in both horizontal directions to contain the largest turbulent eddy. Periodic boundary conditions were implemented in both the streamwise (x) and spanwise (y) directions (Fig. 7). The no-slip boundary condition was applied at the bottom. The free-slip boundary condition

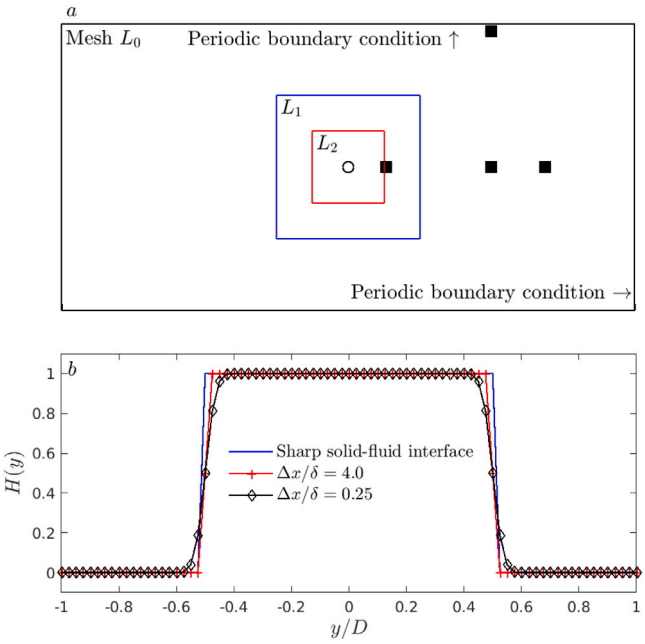

Fig. 7. (a) Sketch of the computational domain with the layout of three levels of grid resolution L_0, L_1 and L_2. The finest grid L_2 is located around the circular cylinder in the center of the computational domain. Periodic boundary conditions are implemented in both horizontal directions. Four sets of probes (square symbols) are placed in the computational domain to obtain time-series of velocity. (b) The smoothed Heaviside function for the circular cylinder. The circular cylinder is located at the center and 1D Heaviside function is shown because of the axis-symmetry of the circular cylinder.

was implemented at the top, in which the gradient of the horizontal velocity components (u and v) is set to zero, and the vertical component of the velocity (w) is set to zero. Uniform grids with two levels of grid refinement were used in the horizontal directions (L_1 and L_2 in Fig. 7a). The coarsest grid size is $\Delta x/H = \Delta y/H = 0.02$, and the finest grid is near the vegetation stem with $\Delta x/H = \Delta y/H = 0.005$. Nonuniform grids are implemented in the vertical direction, with the finest grid near the bottom and $\Delta z_{min}/H = 0.018$. A constant pressure gradient is prescribed to drive the flow. The Reynolds number based on the friction velocity is $Re_\tau = u_* H/\nu = 500$, with u_* as the friction velocity. A fixed time step is used with the maximum CFL number below 0.5.

We first carried out the simulation without the vegetation stem to generate the fully-developed turbulent channel flow. After the simulation reached equilibrium with respect to the turbulence statistics, we placed the swaying vegetation stem at the center of the computational domain ($x = 0$ and $y = 0$). The penalty parameter is set to $D/\epsilon U = 25{,}000$, and the thickness parameter is set to $\Delta x/\delta = 4$.

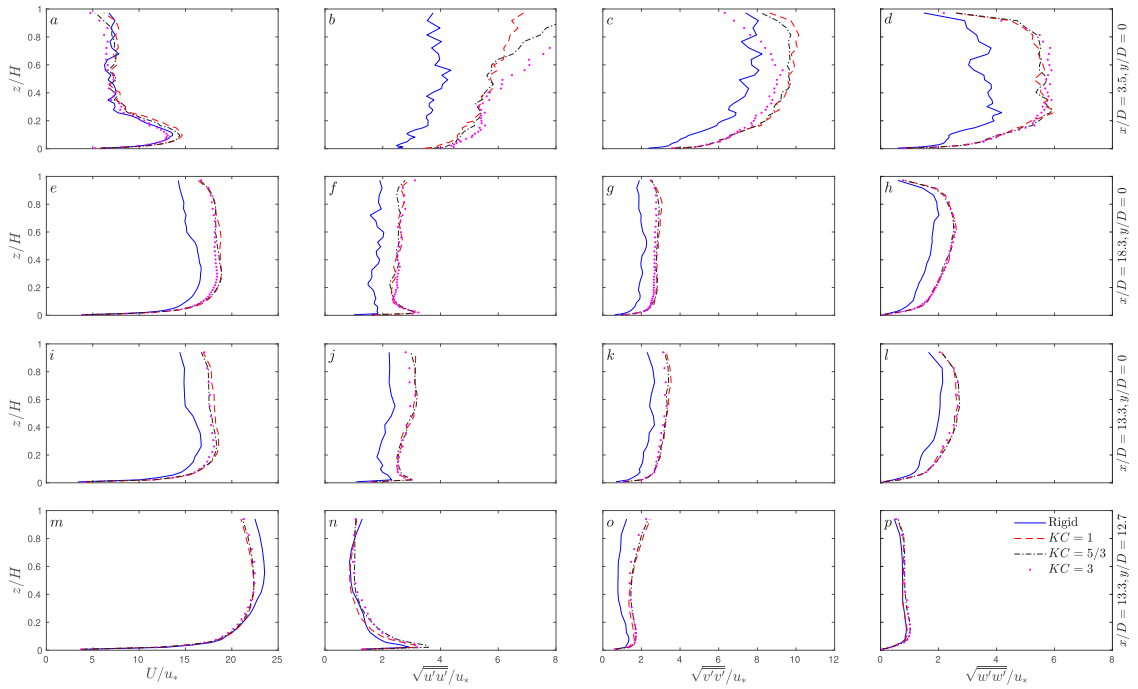

Fig. 8. (a) Mean streamwise (x-) velocity profile (U/u_*), (b) streamwise (x-) component of the turbulent fluctuation ($\sqrt{\overline{u'u'}}/u_*$), (c) spanwise ($y$-) component of the turbulent fluctuation ($\sqrt{\overline{v'v'}}/u_*$), and (d) vertical ($z$-) component of the turbulent fluctuation ($\sqrt{\overline{w'w'}}/u_*$) at $x/D = 3.5$ and $y/D = 0$. (e) to (h) profiles at $x/D = 18.3$ and $y/D = 0$. (i) to (l) profiles at $x/D = 13.3$ and $y/D = 0$. (m) to (p) profiles $x/D = 13.3$ and $y/D = 12.7$.

Fig. 7b shows the mask function for the vegetation stem, and how the thickness parameter δ affects the mask function. The vegetation stem size is $D/H = 0.12$ and 24 horizontal grid points are used to resolve flows around the stem. We keep the angular frequency the same while varying the maximum displacement to get different KC. We first run the simulation for 10 periods for model spin-up, then we continued the simulation for another 20 periods for data analysis.

4.2. Mean flow and turbulence statistics

Four probes were set up in the computational domain to examine the spatial patterns of the flow structure (square symbols in Fig. 7a). Fig. 8 shows the vertical profiles of the streamwise component of the mean velocity U and the root mean square of the velocity fluctuations. Along the center line ($y/D = 0$), at $x/D = 3.5$, the mean velocity profiles show little variation above $z/H = 0.4$ in the wake. Near the wall, the mean velocity first increases, peaks around z/H, and then decreases. The swaying motion of the cylinder has little influence on the mean velocity profiles (Fig. 8a). Compared to the rigid case, the root mean square of turbulent velocity fluctuations are significantly higher in the cases with swaying cylinders (Fig. 8b–d). Turbulent velocity fluctuations only increase slightly with KC because KC is greater than 1 for all cases. At $x/D = 18.3$ along the centerline, both the mean velocity and the turbulent velocity fluctuations in the rigid cylinder case are smaller than the cases with swaying cylinders (Fig. 8e–h). The same pattern can be observed at $x/D = 13.3$ (Fig. 8i–l). Again, the difference among the cases with swaying cylinders is not pronounced due to the range of KC used in this study. At $x/D = 13.3$ and $y/D = 12.7$ (Fig. 8m–p), the mean velocity in the case with a rigid cylinder is greater than the cases with a swaying cylinder, and the spanwise component of the turbulent velocity fluctuation is smaller. The streamwise and vertical components of turbulent fluctuations are only slightly affected by the swaying motion, and the profiles collapse into a single curve. The swaying motion of the cylinder could affect turbulent anisotropy.

Fig. 9 shows the turbulent coherent structures generated by the swaying cylinder. The Q-criterion method (Jeong and Hussain, 1995) is used to visualize the turbulent coherent structures. The horseshoe vortex in front of the stem and braided coherent structures in the wake persist at all phases. At the peak ($\omega t = \pi/2$, Fig. 9b) when the displacement of the cylinder reaches its maximum, the coherent structures are compressed in the wake because it moves in the same direction as the current during $0 < \omega t < \pi/2$. At the trough ($\omega t = 3\pi/2$, Fig. 9d), the coherent structures are stretched in the wake because the cylinder moves in the opposite direction during $\pi < \omega t < 3\pi/2$.

To characterize the turbulence anisotropy, we conducted anisotropy invariant map analysis (Lumley, 1978; Simonsen and Krogstad, 2005). The non-dimensional anisotropy tensor of the Reynolds stress τ_{ij} is defined as

$$b_{ij} = \frac{\tau_{ij}}{\tau_{kk}} - \frac{1}{3}\delta_{ij}, \tag{16}$$

in which δ is the Kronecker Delta.

For incompressible flow, the second (II) and third invariants (III) of the tensor b_{ij} are used. The origin indicates the isotropic turbulence ($II = III = 0$). Fig. 10 compares the anisotropy invariance mapping of two cases, one with a rigid cylinder (Fig. 10a) and the other with a swaying cylinder (Fig. 10b). For both cases, along the center line, we observe the turbulence switches from the axisymmetric at $x/D = 3.5$ to two-component at $x/D = 13.3$. Also, turbulence becomes more isotropic at the center of the domain away from the boundaries. At $x/D = 13.3$ and $y/D = 0$, turbulence falls between two-component and isotropic regimes. With the swaying motion of the cylinder, flow turbulence becomes more isotropic represented by clustered symbols around the origin. The strong anisotropy of turbulence in the case of rigid cylinder suggests the classic Reynolds Averaged Navier–Stokes (RANS) approach with two-equation turbulence closure may fail to accurately predict the turbulent characteristics and hence the turbulent mixing, due to the scalar eddy viscosity in the model. The Reynolds Stress Model (RSM) approach may work better with flow over emergent vegetation canopy.

4.3. Bottom shear stress

Fig. 11a shows the time-averaged bottom shear stress for the case with a rigid stem. Large eddy simulation resolves both wall-generated

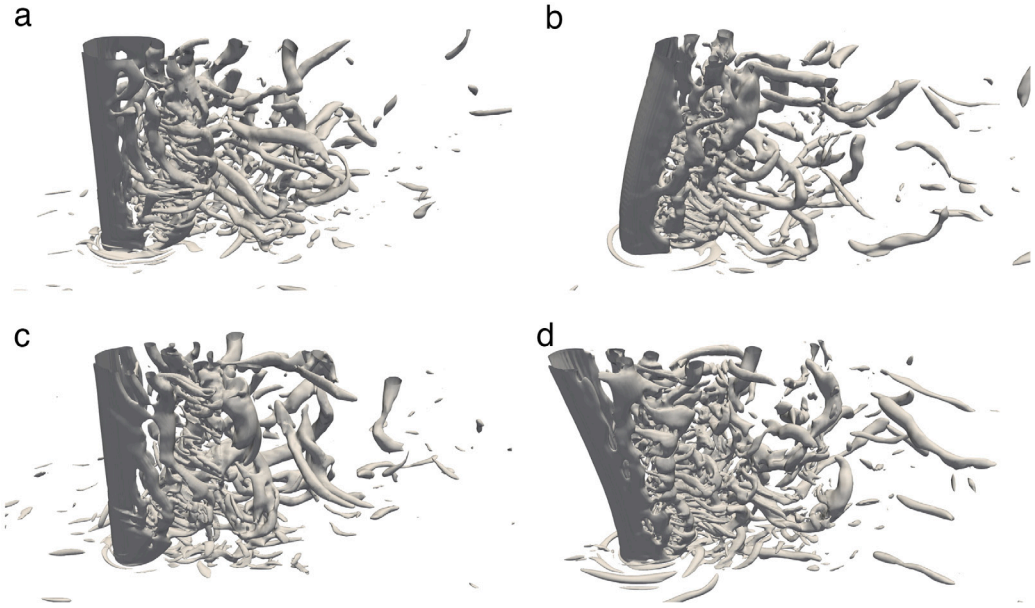

Fig. 9. Turbulent coherent structures for the case with $KC = 1$ at four different phases. (a) Acceleration $\omega t = 0$, (b) peak $\omega t = \pi/2$, (c) deceleration $\omega t = \pi$, and (d) trough $\omega t = 3\pi/2$.

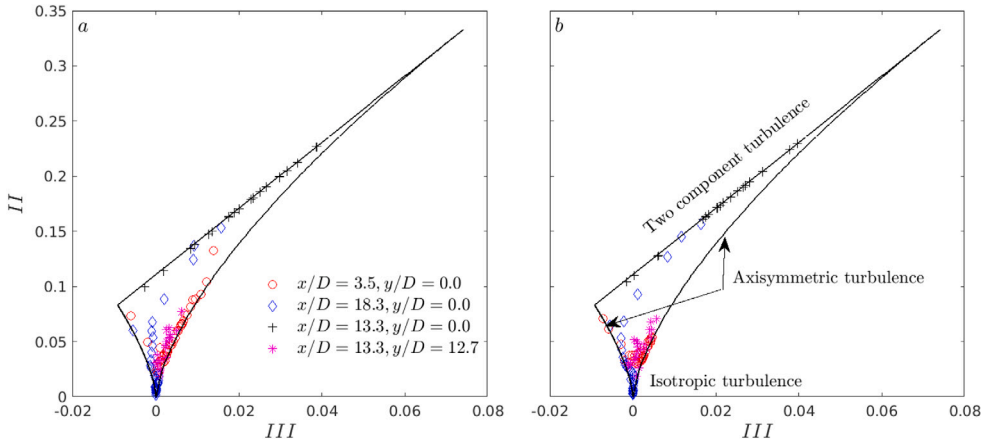

Fig. 10. The anisotropy invariance mapping for the case with (a) a rigid cylinder and (b) a swaying cylinder with $KC = 1$.

turbulence and stem-generated turbulence, and hence the bottom shear stress includes interactions of both wall-generated turbulent eddies and stem-generated eddies with the bed. Regions of large bottom shear stress can be observed at shoulders of the stem. In the wake of the stem, a region with negative shear stress close to the stem exists, followed by a region with large shear stress. Fig. 11b shows the comparison of the spatially averaged bottom shear stress for all cases. The bottom shear stress is averaged in the spanwise (y-) direction, and normalized by $\tau_0 = \rho u_*^2$. For all cases, the bottom shear stress increases and peaks at the center of the stem, then it decreases in the wake. The bottom shear stress increases and reaches the asymptotic value in bare channel outside of the recirculation zone behind of the stem. The bottom shear stress at the shoulders of the circular cylinder is around 5% larger in cases with a swaying cylinder compared to the case with a rigid stem, suggesting enhanced erosion by the swaying motion of the vegetation stem. Because of the range of Keulegan Carpenter numbers ($KC \geq 1$) used in the study, the difference between cases with a swaying cylinder is not pronounced. A small increase of τ/τ_0 can be observed in the wake of the cylinder for the case with the largest KC.

4.4. Drag force

The hydrodynamic force acting on the vegetation stem can be computed by integrating the stress tensor (including both the viscous stress and pressure) over the surface

$$\mathbf{F} = \iint \tau \cdot \mathbf{n} dA, \tag{17}$$

in which $\mathbf{n}$ is the unit surface normal vector. In volume penalization immersed boundary method, the stress tensor (τ) is continuous across the fluid–solid interface and hence τ is interpolated at the interface to compute the drag force.

Fig. 12a shows the vertical profile of the time-averaged drag coefficient $C_D = f/(0.5\rho A\bar{U}^2)$. The drag coefficient is calculated at the vertical elevation $z = (z_1+z_2)/2$, the projected area in the flow direction is $A = D\Delta z$ with $\Delta z = (z_2 - z_1)$, and $\bar{U}$ is the depth-averaged velocity. Results from cases with different KC show a similar pattern. Drag coefficient first increases with the vertical elevation z/H, approaches a constant value around 1 between z/H of 0.2 and 0.6, and then drops towards the top of the domain. The flow velocity past the cylinder is smaller in the bottom boundary layer than the depth-averaged velocity, so the drag coefficient is smaller in the bottom boundary layer. The

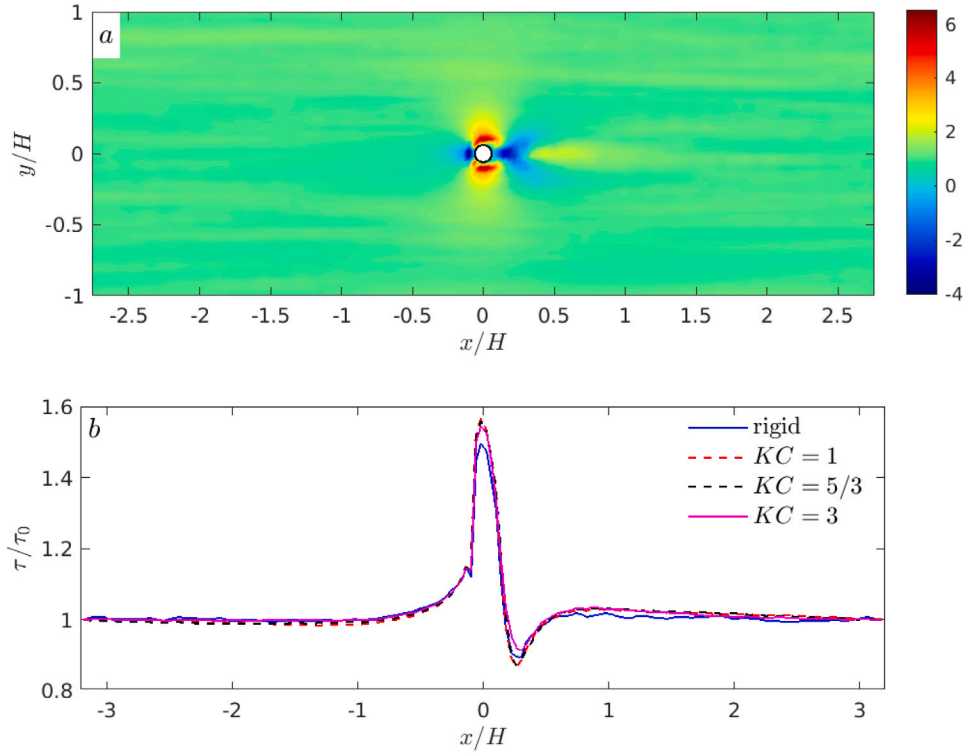

Fig. 11. (a) The time-averaged bottom shear stress for the case with rigid stems. (b) The normalized bottom shear stress profiles averaged in time and spanwise $y-$ direction.

swaying motion of the cylinder generates a self-induced wake zone that oscillates with the cylinder. The wake is strongest at the top because the displacement is at its largest. The flow sheltering due to the self-induced wake generated by the swaying motion leads to the drag reduction. Overall, the drag reduction increases with KC (Fig. 12a). The drag reduction also varies vertically. Close to the bottom, the maximum displacement is relatively small compared to the stem size, and the drag force is not significantly affected by the self-induced wake of the swaying stem. Far away from the bottom, effects of the self-induced wake become increasingly important. Fig. 12b and c show the phase-averaged drag coefficient at two vertical elevations. At $z/H = 0.6$, the peak of the drag coefficient occurs at $\omega t = \pi$ when the velocity of the swaying cylinder reaches its peak. The drag coefficient is symmetric at $\omega t = \pi$ with a peaky crest and flat trough with $KC = 5/3$ and 3. The drag coefficient does not vary much with $KC = 1$. At $z/H = 1$, the variation of the drag coefficient within one wave cycle increases with KC. The peak of the drag coefficient is not at $\omega t = \pi$ anymore, the phase lag might be due to the strong self-induced wake of the cylinder.

5. Effect of swaying motion of vegetation on patch-scale flow structures

Aquatic vegetation often form patches due to clonal growth (Sand-Jensen and Madsen, 1992). Hydrodynamics over a patch of vegetation strongly depend on the patch properties, including the solid volume fraction (ϕ), size and shape. For a circular vegetation patch, at low solid volume fraction ($\phi < 5\%$), each individual stem behaves like an isolated vegetation stem (Nicolle and Eames, 2011). At intermediate to high solid volume fraction ($\phi > 0.05$), patch-scale wake billows form in the wake of the vegetation patch (Chang and Constantinescu, 2015), which is similar to the von Karman vortex street behind a solid structure with the same size and shape. We assume dense emergent vegetation shields the water surface from wind and attenuates surface waves, only effects of swaying motion of vegetation on steady currents are investigated. Particularly, we focus on how the swaying motions of vegetation stems affect the velocity structure and the turbulent transport in dense emergent vegetation canopies.

We conducted numerical simulations of flow over dense patches of vegetation. The computation domain size is $6.4H \times 3.2H \times H$, where H is the channel height. A nearly circular patch of vegetation consisted of 19 stems is located at the center of the domain. The stems are regularly spaced in a hexagonal pattern and the centers of the circular cylinders are aligned along the y (spanwise) direction (see 13a). The diameter of the circular patch is set to $D_p/H = 0.8$. The solid volume fraction is varied by changing the diameter of the vegetation stems. Two volume fractions were chosen as $\phi = 11.75\%$ (intermediate) and 32.65% (high), respectively. Simulations with both rigid and swaying vegetation stems were carried out to understand how the swaying motions affect the patch-scale dynamics. The maximum excursion of the vegetation stem δ_{max} was set to $0.2H$ for all simulations.

Periodic boundary conditions were implemented in both the streamwise (x-) and spanwise (y-) directions. The model setup can be interpreted as the flow over infinite arrays of regularly-spaced circular patches. At the bottom, the no-slip boundary condition was implemented. Free-slip boundary condition was implemented at the top, in which gradients of lateral velocities are set to zero, and the vertical velocity is set to zero. Two levels of grid refinement were implemented with the finest grid of $\Delta x/H = \Delta y/H = 0.005$. One vegetation stem is resolved by 24 horizontal grids for the case with high solid volume fraction ($\phi = 32.65\%$) and 16 horizontal grids for the case with intermediate solid volume fraction ($\phi = 11.75\%$). A constant pressure gradient was implemented to drive the steady current and maintain the same mean velocity U_{mean}. The Reynolds number based on the frictional velocity is $Re_\tau = 500$. A constant time step was used with $CFL \leq 0.5$ for all cases. Simulations with swaying vegetation reached the equilibrium in 10 wave cycles. Therefore, the first 10 wave cycles of each simulation were model spin-ups and not used for the analysis. After spin up, we continued the simulations for another 20 wave cycles to compute flow and turbulence statistics.

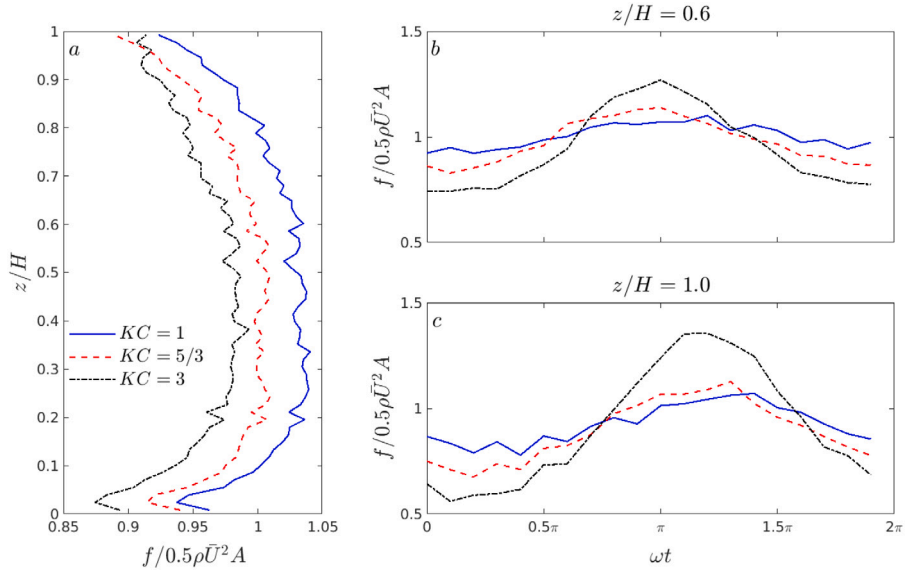

Fig. 12. (a) Vertical profile of the time-averaged drag coefficient. The time history of the drag coefficient at (b) $z/H = 0.6$ and (c) $z/H = 1$.

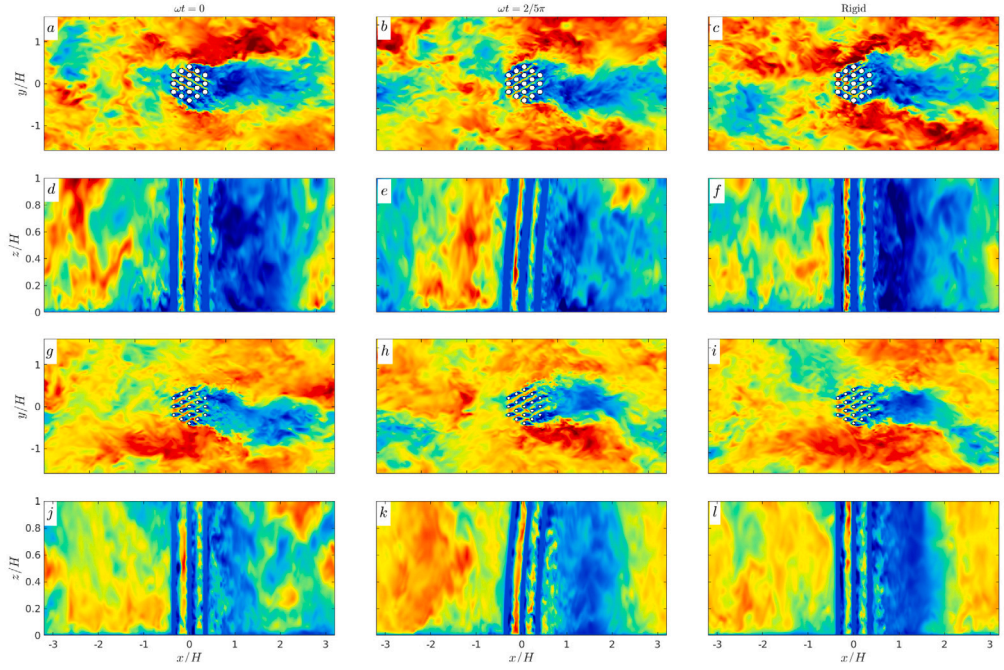

Fig. 13. Instantaneous velocity field, the background color shows the normalized streamwise velocity component u/U_{mean}. Horizontal slice $(x-y)$ from cases with high solid volume fraction of $\phi = 32.65\%$ at (a) $\omega t = 0$, (b) $\omega t = 2/5\pi$, and (c) rigid stems. Vertical slice $(x-z)$ at (d) $\omega t = 0$, (e) $\omega t = 2/5\pi$, and (f) rigid stems. Horizontal slice $(x-y)$ from cases with low solid volume fraction of $\phi = 11.75\%$ at (g) $\omega t = 0$, (h) $\omega t = 2/5\pi$, and (i) rigid stems. Vertical slice $(x-z)$ at (j) $\omega t = 0$, (k) $\omega t = 2/5\pi$, and (l) rigid stems.

5.1. Flow kinematics

Fig. 13 shows the instantaneous flow fields at different phases ($\omega t = 0$ and $2/5\pi$). At high solid volume fraction ($\phi = 32.65\%$), the vegetation patch behaves like a solid cylinder. At $\omega t = 0$, the recirculation zone in the case with swaying vegetation stems (Fig. 13a and d) is slightly larger compared to the case with rigid stems (Fig. 13c and f). At $\omega t = 2/5\pi$, the vegetation stems push the fluid forward, and the wake structure varies strongly vertically (Fig. 13e) because the prescribed velocity of the stems increases with z/H. At intermediate solid fraction ($\phi = 11.75\%$), similar patterns can be observed, and the size of the recirculation zone is smaller than the case with larger solid volume fraction.

To examine how the swaying motion affects the patch-scale vortex shedding, we extracted the instantaneous spanwise (v-component) velocity at $x/D_p = 2.25$ and $z/H = 0.25$. Upper panels in Fig. 14 show the time–history of the spanwise velocity (v), and the energy spectrums are shown in the lower panels. At high solid volume fraction, the Strouhal number peaks near $St \approx 0.25$ in both rigid and swaying cases, and the shedding frequency is similar to that of flow past a solid circular cylinder. For the case with swaying stems (Fig. 14g), we did not observe the peak at $St = 0.1$, which is the frequency of the swaying motion of individual stems. The swaying motion does not affect the shedding frequency of the large patch-scale eddies. For cases with intermediate solid volume fraction (Fig. 14f), a peak around $St = 0.13$ can be identified. A second peak around the second harmonic $St = 0.26$ can also be identified for the case with rigid stems. With swaying stems,

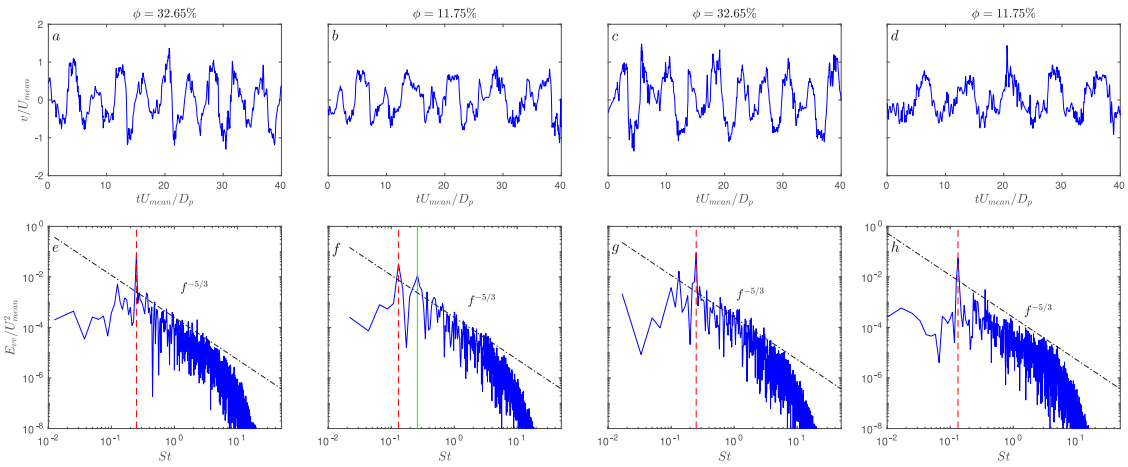

Fig. 14. Time–history of instantaneous spanwise velocity v/U_{mean} at $x/D_p = 2.25$ and $z/H = 0.25$. (a) Rigid stems with solid volume fraction of 32.65%. (b) Rigid stems with solid volume fraction of 11.75%. (c) Swaying stems with solid volume fraction of 32.65%. (d) Swaying stems with solid volume fraction of 11.75%. The corresponding energy spectrum of the spanwise velocity E_{vv}/U^2_{mean}: (e) Rigid stems with solid volume fraction of 32.65%. (f) Rigid stems with solid volume fraction of 11.75%. (g) Swaying stems with solid volume fraction of 32.65%. (h) Swaying stems with solid volume fraction of 11.75%.

the time history of the spanwise velocity shows a nonlinear saw-tooth shape. Only a single peak at $St = 0.133$ can be identified in the normalized energy spectrum. For all cases, the $-5/3$ slope is evident, suggesting the LES model can resolve the inertial subrange reasonably well with given grid resolution.

5.2. Turbulence statistics

At $x/D_p = 2$, the flow is dominated by the large-scale billows. The frequency of the swaying motion does not show up as in Fig. 14. Time-average is therefore used to separate the mean velocity from the turbulent fluctuations, instead of the phase-average. Fig. 15a shows the vertical profiles of the normalized mean stream velocity at $y/D_p = 1.9$. The mean velocity profiles converge for cases with large volume fraction. For cases with intermediate volume fraction, the mean velocity is smaller with swaying stems at $z/H < 0.5$. For cases with high solid volume fraction, all three turbulent fluctuation components are smaller when the swaying motions of the stems are included (Fig. 15b to d). For cases with intermediate solid volume fraction, the spanwise component velocity fluctuation is significantly enhanced by the swaying motion of the stems (Fig. 15c), while both the streamwise component (Fig. 15b) and the vertical component (Fig. 15d) are attenuated.

Along the center line ($y/D_p = 0$), large velocity defect of the mean velocity can be observed in the wake (Fig. 15e). The velocity defect is smaller for the case of intermediate solid volume fraction with swaying stems. The swaying motion of the stems has little effect on the turbulent fluctuations for both cases (Fig. 15f to h). However, the solid volume fraction significantly affects the spanwise and the vertical components of the turbulent fluctuations, both of which increase with the solid volume fraction (Fig. 15g and h). Dense vegetation patch behaves similar to a porous solid cylinder with a large-patch scale wake. An effective Keulegan–Carpenter number can be defined as the ratio of the excursion δ_{max} to the size of the patch D_p, which is $KC = 0.25$. At low KC, effects of the swaying motion of vegetation stems on turbulent generation is expected to be weak.

5.3. Bottom shear stress

The time-averaged normalized bottom shear stresses from cases with rigid stems are presented in Fig. 16 panel a and b. Regions with high bottom shear stress can be observed in the gaps between vegetation stems in both cases, as well as the shoulders of the patch due to the formation of patch-scale shear layer at the shoulders. Because the interstitial space in the case with low solid volume fraction is greater, the averaged bottom shear stress decreases with increasing ϕ for dense vegetation patch. The bottom shear stress decreases in the wake for both cases. For the case with high solid volume fraction ($\phi = 32.65\%$), a region with negative bottom shear stress at $x/D_p \approx 1.6$ ($x/H \approx 1.3$) can be observed in the wake of the patch.

The time-averaged bottom shear stress (Fig. 16c) is averaged in the spanwise (y-) direction, and normalized by $\tau_0 = \rho u_*^2$. For all cases, the bottom shear stress increases and reaches the maximum at the center of the patch with several peaks in the vegetation patch because the vegetation stems are aligned along the y direction. For cases with high volume fraction, the bottom shear stress decreases in the wake of the patch with a minimum, and then increases and approaches the asymptotic value in bare channel outside of the patch-scale recirculation zone. For the case with intermediate volume fraction, the bottom shear stress shows a smooth decrease in the wake and then reaches the asymptotic value. By including the swaying motion, the bottom shear stress increases by up to 4%, with the maximum value at the shoulders of the patch. The effect of the swaying motions on the bottom shear stress is not significant.

5.4. Drag force

The time-averaged non-dimensional drag force acting on the solid cylinder within the array $\vec{F}/(0.5\rho U^2_{mean} D)$ gives information on both the magnitude and orientation of the total drag force on a particular cylinder (Fig. 17). The direction of the total drag force on a particular cylinder is a good indicator of the direction of the local flow in the gap between cylinders. No significant difference is evident by including the swaying motion of the stems. The solid volume fraction is greater than 5% in both cases, and the patch behaves as a porous cylinder with formation of patch-scale wake billows (Fig. 13). The magnitude of the force acting on cylinders is largest at the leading edge of the patch (cylinders 1 to 3) due to the direct exposure to the incoming flow. Large forces can also be observed on cylinders 8 and 12, where the separated shear layer forms with high velocity at the shoulders of the porous patch. For both cases, the bleeding flow within the porous patch has a lateral component, which follows the separated shear layer. The drag force on cylinders decreases away from the upstream side of the patch, and the decay is more pronounced for the case with a larger solid volume fraction. Strong flow sheltering can be observed at the trailing edge of the vegetation patch, where the drag forces are significantly smaller due to the small effective KC number in our simulations.

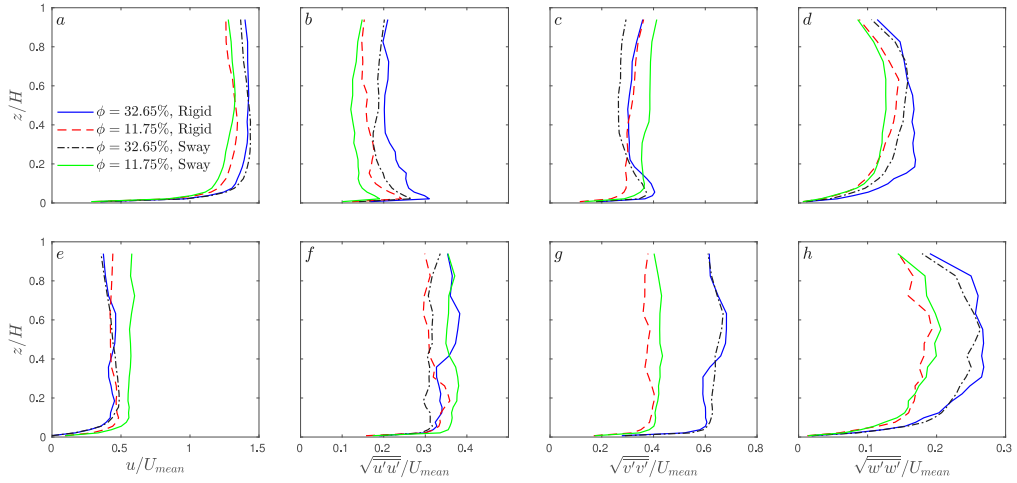

Fig. 15. Time-average vertical profiles at $x/D_p = 2$ and $y/D_p = 1.9$. (a) normalized mean velocity, (b) normalized streamwise velocity fluctuation, (c) normalized spanwise velocity fluctuation, (d) normalized vertical velocity fluctuation. Vertical profiles at $x/D_p = 2$ and $y/D_p = 0$. (e) normalized mean velocity, (f) normalized streamwise velocity fluctuation, (g) normalized spanwise velocity fluctuation, (h) normalized vertical velocity fluctuation.

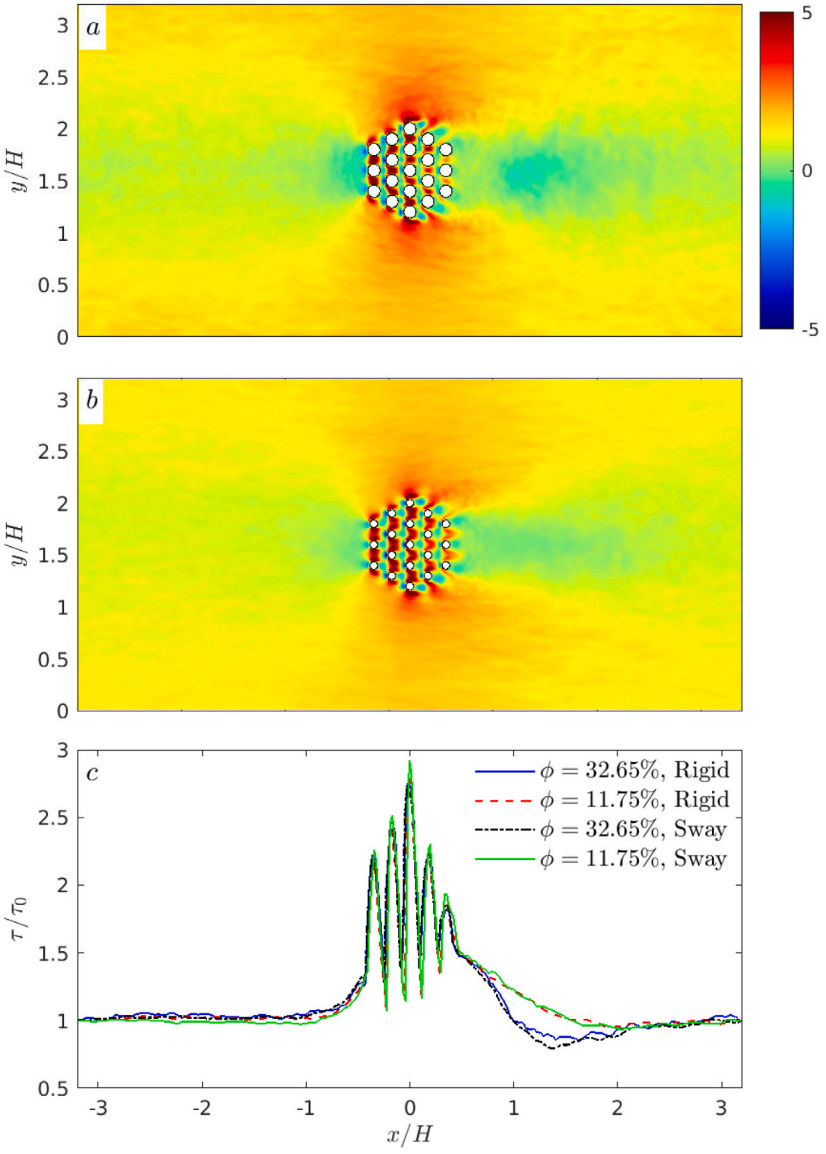

Fig. 16. (a)The time-averaged normalized bottom shear stress for the case with $\phi = 32.65\%$ and rigid stems. (b) Time-averaged normalized bottom shear stress for the case with $\phi = 11.75\%$ and rigid stems. (c) The normalized bottom shear stress profiles for all cases. The spatial average is taken in the spanwise (y) direction.

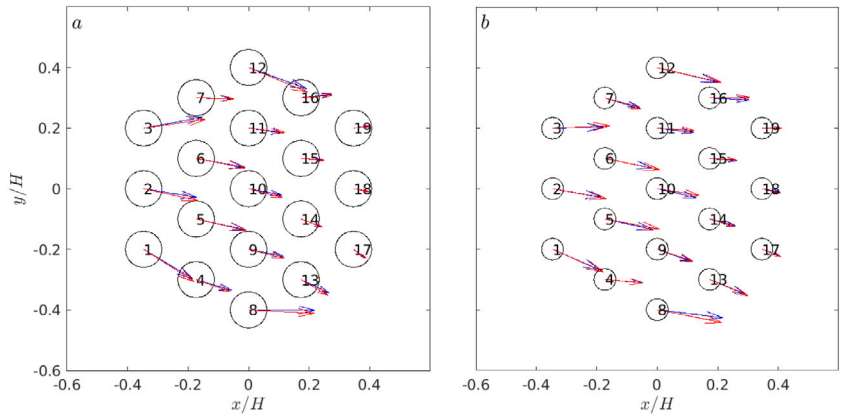

Fig. 17. (a) The time-averaged normalized drag force on each individual stems for the case with $\phi = 32.65\%$. (b) Time-averaged normalized drag force on each individual stems for the case with $\phi = 11.75\%$. The blue arrows represent results from cases with rigid cylinders, and the red arrows represent results from cases with swaying cylinders.

5.5. Application of sediment transport

The large eddy simulation model resolves all the relevant turbulent eddies, including wall-generated turbulent eddies, stem-generated turbulent eddies and large patch-scale turbulent eddies. Vegetation generated turbulent eddies are the main drivers of sediment transport in emergent vegetation canopy (Tinoco and Coco, 2013; Yang et al., 2016). In LES models, the bottom shear stress includes interactions of both wall-generated and vegetation-generated turbulent eddies with the sediment bed. Sediment transport pattern can therefore be directly linked with the spatial distribution of bottom shear stress predicted by LES model, in which regions with large bottom shear stress are more likely to be associated with erosion. Large bottom shear stress can be observed at the shoulders of the patch. The shear stress is larger in the case with high solid volume fraction due to stronger flow blockage by the vegetation patch. Regions of large bottom shear stress can also be observed in the gaps between vegetation stems inside of the vegetation patch, suggesting stronger sediment resuspension may occur in the vegetation canopy. The shear stress in the vegetation canopy decreases away from the upstream leading edge of the patch. In addition, the area of regions with high bottom shear stress between vegetation stems is larger in the case of intermediate solid volume fraction (Fig. 16b).

In classic sediment transport model, Rouse profile is widely used to model the transport of suspended sediment. In the Rouse model, the shear stress profile is assumed to be linear following the logarithmic law of the velocity distribution, and the turbulent diffusion is modeled by a parabolic profile (Hunter, 1938). The Rouse model is based on turbulent channel flow and only considers interactions of suspended sediment particles with wall-generated turbulent eddies. However, in emergent vegetation canopy, vegetation generated turbulence also plays an important role in the vertical distribution of suspended sediment. At stem-scale, the swaying motion of vegetation stems significantly enhances the stem-generated turbulence (Fig. 8), and hence the turbulent diffusion. At patch-scale, due to the small effective Keulegan Carpenter number, the turbulence enhancement is not pronounced and mainly occurs in the wake. A revisited suspended sediment transport model that considers vegetation generated turbulence needs to be developed to improve the prediction of suspended sediment transport in regions with emergent aquatic vegetation.

6. Conclusion

A volume-penalization immersed boundary (VPIB) method was developed to study flow interactions with aquatic vegetation, in which vegetation stems are modeled as porous solid objects. The VPIB method can be efficiently implemented in existing computational model framework with minimum effort. With the implicit treatment of the source term, the time step is not restricted by the penalty parameter. The primary shortcoming of the VPIB method is the smoothing of the sharp interface, which affects the model accuracy on the boundary. The model has been validated with data from laboratory experiment and previous high fidelity models of turbulent flow over a circular cylinder, flow generated by an oscillating cylinder at low Keulegan–Carpenter number and flow over circular patches of rigid cylinders with satisfactory model performance. Sensitivity analyzes of the penalty parameter and thickness parameter were carried out. The optimal value of the thickness parameter was recommended based on the size of the computational grid. The optimal value of penalty parameter should be chosen on a case-by-case basis.

Effects of the swaying motion of vegetation on the hydrodynamics were investigated at both the stem and patch scale by forcing the stems with a simplified prescribed motion. At stem-scale, we conducted simulations with three different Keulegan Carpenter numbers (KC equals to 1, 1.67 and 3), in which the Keulegan Carpenter number is defined as the maximum excursion of the vegetation stem to the diameter of the vegetation stem. We observed the enhancement of the turbulent generation in the wake of the vegetation stem in all cases when the swaying motion is introduced. In addition, the swaying motions of stems resulted in more isotropic turbulence. The time-averaged bottom shear stress is only slightly enhanced (around 5%) at the shoulders of the stem by the swaying motion, the effect is negligible in the wake. This could be due to the prescribed motion of the vegetation stem, which decreases to zero at the bed following a cubic law of the vertical elevation from the bed. The time-averaged drag coefficient based on the depth-averaged flow velocity decreases with the Keulegan–Carpenter number slightly due to flow sheltering from the self-induced wake by the swaying motion.

We focused on steady currents over a dense vegetation patch, which shields the water surface from wind. For vegetation patch with intermediate or high solid volume fraction, large patch-scale wake billows form in the wake of the vegetation patch. The hydrodynamics strongly depend on the solid volume fraction and the effective Keulegan Carpenter number based on the patch size. At high solid volume fraction, the shedding frequency is similar to that of flow past a solid circular cylinder for both cases with rigid and swaying stems. At intermediate solid volume fraction, Strouhal number peaks around 0.133, which is smaller than the value based on the vortex shedding frequency of a solid cylinder. A second peak around the vortex shedding frequency appears in the case with rigid stems, which is not evident in the case with swaying stems. Effects of the swaying motion on the patch-scale velocity and turbulence statistics are not significant. The swaying motion of vegetation stems enhances the size of the recirculation zone and the turbulence generation in the wake. The enhancement in the streamwise component of the turbulent fluctuation is more pronounced compared

to the spanwise and the vertical components. The effects of swaying motion on turbulence generation are negligible outside of the wake. The effect of swaying motion is insignificant for the bottom shear stress. For the dense vegetation patch, the patch-scale hydrodynamics strongly depend the effective Keulegan Carpenter number based on the patch size, instead of the Keulegan Carpenter number based on stem size. The effects of swaying motion on the patch-scale hydrodynamics are not pronounced due to the small effective KC number. The distribution of the time-averaged drag coefficient on the vegetation stem in the canopy depends on the patch-scale flow, and the effect of swaying motion on the drag coefficient on individual stems is not pronounced again due to the small effective Keulegan–Carpenter number.

CRediT authorship contribution statement

Xiao Yu: Supervision, Conceptualization, Methodology, Formal analysis, Writing – original draft, Writing – review & editing. **Minglan Yu:** Software, Model validation, Formal analysis, Writing – original draft, Writing – review & editing.

Declaration of competing interest

The authors declare that they have no known competing financial interests or personal relationships that could have appeared to influence the work reported in this paper.

Acknowledgments

This work is funded by the National Science Foundation, United States (Hydrologic Sciences program 1945685). All simulations were carried out on the HiperGator super computer at the University of Florida. Computer resources, technical expertise and assistance provided by the HiperGator are gratefully acknowledged. The CFD model OpenFOAM is developed primarily by the OpenCFD Ltd at https://www.openfoam.com/.

References

Akiki, G., Balachandar, S., 2016. Immersed boundary method with non-uniform distribution of lagrangian markers for a non-uniform eulerian mesh. J. Comput. Phys. 307, 34–59.

Augustin, L.N., Irish, J.L., Lynett, P., 2009. Laboratory and numerical studies of wave damping by emergent and near-emergent wetland vegetation. Coast. Eng. 56 (3), 332–340.

Berndt, M., Breil, J., Galera, S., Kucharik, M., Maire, P.H., Shashkov, M., 2011. Two-step hybrid conservative remapping for multimaterial arbitrary lagrangian–eulerian methods. J. Comput. Phys. 230 (17), 6664–6687.

Chang, K., Constantinescu, G., 2015. Numerical investigation of flow and turbulence structure through and around a circular array of rigid cylinders. J. Fluid Mech. 776 (161).

Chen, Z., Ortiz, A., Zong, L., Nepf, H., 2012. The wake structure behind a porous obstructionand its implications for deposition near a finite patch of emergent vegetation. Water Res. Res. 48 (9).

Chen, Q., Qi, M., Zhong, Q., Li, D., 2017. Experimental study on the multimodal dynamics of the turbulent horseshoe vortex system around a circular cylinder. Phys. Fluids 29 (1), 015106.

Craft, C.J., Clough, J., Ehman, J., Joye, S., Park, R., Pennings, S., Machmuller, M., 2009. Forecasting the effects of accelerated sea-level rise on tidal marsh ecosystem services. Front. Ecol. Environ. 7 (2), 73–78.

Dutsch, H., Durst, F., Lienhart, H., 1998. Low-reynolds-number flow around an oscillating circular cylinder at low keulegan–carpenter numbers. J. Fluid Mech. 360, 249–271.

Engels, T., Kolomenskiy, D., Schneider, K., Sesterhenn, J., 2015. Numerical simulation of fluid?structure interaction with the volume penalization method. J. Comput. Phys. 281, 96–115.

Gedan, K.B., Kirwan, M.L., Wolanski, E., Barbier, E.B., Silliman, B.R., 2011. The present and future role of coastal wetland vegetation in protecting shorelines: answering recent challenges to the paradigm. Clim. Change 106 (1), 7–29.

Gedan, K.B., Silliman, B.R., Bertness, M.D., 2009. Centuries of human-driven change in salt marsh ecosystems. Annu. Rev. Mar. Sci. 1, 117–141.

Glowinski, R., Pan, T.W., Periaux, J., 1994. A fictitious domain method for dirichlet problem and applications. Comput. Methods Appl. Mech. Engrg. 111 (3–4), 283–303.

Hirt, C.W., Amsdena, A.A., Cook, J.L., 1974. An arbitrary lagrangian-eulerian computing method for all flow speeds. J. Comput. Phys. 14 (3), 227–253.

Huai, W., Xue, W., Qian, Z., 2015. Large-eddy simulation of turbulent rectangular open-channel flow with an emergent rigid vegetation patch. Adv. Water Resour. 80, 30–42.

Hunter, Rouse, 1938. Experiments on the mechanics of sediment suspension. In: Proc. 5th Int'L. Congress for Applied Mechanics, Cambridge, Mass.

Jeong, J., Hussain, F., 1995. On the identification of a vortex. J. Fluid Mech. 285, 69–94.

Kadoch, B., Kolomenskiy, D., Schneider, K., 2012. A volume penalization method for incompressible flows and scalar advection–diffusion with moving obstacles. J. Comput. Phys. 231 (12), 4365–4383.

Kim, D.H., Yang, K.S., Senda, M., 2004. Large eddy simulation of turbulent flow past a square cylinder confined in a channel. Comput. & Fluids 33 (1), 81–96.

Kravchenko, A.G., Moin, P., 2000. Numerical studies of flow over a circular cylinder at Re=3900. Phys. Fluids 12 (2), 403–417.

Kremen, C., 2005. Managing ecosystem services: what do we need to know about their ecology? Ecol. Lett. 5, 468–479.

Lee, I., Choi, H., 2015. A discrete-forcing immersed boundary method for the fluid–structure interaction of an elastic slender body. J. Comput. Phys. 280, 529–546.

Lourenco, L.M., 1993. Characteristics of the plane turbulent near wake of a circular cylinder, A particle image velocimetry study.

Lumley, 1978. Computational modelling of turbulent flows. Adv. Appl. Mech. 18 (123).

Marani, M., dÁlpaos, A., Lanzoni, S., Santalucia, M., 2011. Understanding and predicting wave erosion of marsh edges. Geophys. Res. Lett. 38 (21).

Micheli, E.R., Kirchner, J.W., 2002. Effects of wet meadow riparian vegetation on streambank erosion 2. measurements of vegetated bank strength and consequences for failure mechanics. Earth Surf. Process. Landf. J. Br. Geomorphol. Res. Group 27 (2), 687–697.

Mittal, R., Iaccarino, G., 2005. Immersed boundary methods. Annu. Rev. Fluid Mech. 37, 239–261.

Nepf, H.M., 1999. Drag, turbulence, and diffusion in flow through emergent vegetation. Water Resour. Res. 35 (2), 479–489.

Nicolle, A., Eames, I., 2011. Numerical study of flow through and around a circular array of cylinders. J. Fluid Mech. 679, 1–31.

Parnaudeau, P., Carlier, J., Heitz, D., Lamballais, E., 2008. Experimental and numerical studies of the flow over a circular cylinder at reynolds number 3900. Phys. Fluids 20 (8), 085, 101.

Parussini, L., Pediroda, V., 2009. Fictitious domain approach with hp-finite element approximation for incompressible fluid flow. J. Comput. Phys. 228 (10), 3891–3910.

Peskin, C.S., 2002. The immersed boundary method. Acta Numer. 11, 479–517.

Piquet, A., Roussel, O., Hadjadj, A., 2016. A comparative study of brinkman penalization and direct-forcing immersed boundary methods for compressible viscous flows. Comput. & Fluids 136, 272–284.

Sand-Jensen, K.A.J., Madsen, T.O.M.V., 1992. Patch dynamics of the stream macrophyte, callitriche cophocarpa. Freshwater Biol. 27 (2), 277–282.

Shan, Y., Zhao, T., Liu, C., Nepf, H., 2020. Turbulence and bed load transport in channels with randomly distributed emergent patches of model vegetation. Geophys. Res. Lett. 47 (12), e2020GL087055.

Simonsen, A.J., Krogstad, P.-Å., 2005. Turbulent stress invariant analysis: Clarification of existing terminology. Phys. Fluids 17 (8), 0088, 103.

Stoesser, T., Kim, S.J., Diplas, P., 2010. Turbulent flow through idealized emergent vegetation. J. Hydraul. Eng. 136 (12), 1003–1017.

Tanino, Y., Nepf, H.M., 2008. Laboratory investigation of mean drag in a random array of rigid, emergent cylinders. J. Hydraul. Eng. 134 (1), 34–41.

Tinoco, R.O., Coco, G., 2013. Observations of the effect of emergent vegetation on sediment resuspension under unidirectional currents and waves. Earth Surf. Dyn. Discuss. 1 (1), 601–636.

Tseng, Y.-H., Ferziger, J.H., 2003. A ghost-cell immersed boundary method for flow in complex geometry. J. Comput. Phys. 192 (2), 593–623.

Uhlmann, M., 2005. An immersed boundary method with direct forcing for the simulation of particulate flows. J. Comput. Phys. 209 (2), 448–476.

Wang, X., Liu, W.K., 2004. Extended immersed boundary method using fem and rkpm. Comput. Methods Appl. Mech. Engrg. 193 (12–14), 1305–1321.

Weller, H.G., Tabor, G., Jasak, H., Fureby, C., 1998. A tensorial approach to computational continuum mechanics using object-oriented techniques. Comput. Phys. 12 (6), 620–631.

Yang, J.Q., Chung, H., Nepf, H.M., 2016. The onset of sediment transport in vegetated channels predicted by turbulent kinetic energy. Geophys. Res. Lett. 43 (21), 11–261.

Zedler, E.A., Street, R.L., 2001. Large-eddy simulation of sediment transport: currents over ripples. J. Hydraul. Eng. 127 (6), 444–452.

Zhao, M., Cheng, L., Zang, Z., 2010. Experimental and numerical investigation of local scour around a submerged vertical circular cylinder in steady currents. Coast. Eng. 57 (8), 709–721.

Zong, L., Nepf, H., 2012. Vortex development behind a finite porous obstruction in a channel. J. Fluid Mech. 691, 368–391.